Multi-Frequency Spherical Near-Field Antenna Measurements Using Compressive Sensing

Marc Andrew Valdez, Jacob D. Rezac, Michael B. Wakin, *Fellow, IEEE*, and Joshua A. Gordon

***Abstract*—We propose compressive sensing approaches for broadband spherical near-field measurements that reduce measurement demands beyond what is achievable using conventional single-frequency compressive sensing. Our approaches use two different compressive signal models—sparsity-based and low-rank-based—whose viability we establish using a simulated standard gain horn antenna. Under mild assumptions on the device being tested, we prove that sparsity-based broadband compressive sensing provides significant measurement number reductions over single-frequency compressive sensing. We find that our proposed low-rank model also provides an effective means of achieving broadband compressive sensing, using numerical experiments, with performance on par with the best broadband sparsity-based method. Exemplifying these best-case results, even in the presence of measurement noise, the methods we propose can achieve relative errors of -40 dB using about 1/4 of the measurements required for conventional sampling. This is equivalent to about 1/2 sample per unknown, whereas traditional spherical near-field measurements require a minimum of roughly 2 measurements per unknown.**

***Index Terms*—Compressed sensing, antenna radiation patterns, broadband antennas, antenna measurements, near-field radiation pattern.**

I. Introduction

CHARACTERIZING the near- or far-field radiation pattern [1] of an antenna or antenna array is critical for understanding antenna performance. Such characterizations allow antennas to be properly considered in performance models and help to identify undesirable device performance characteristics. Communications devices that operate on 5G and future 6G modalities incorporate technologies such as beamforming, beamsteering, and field controllability that complicate radiation pattern characterization. These devices operate in a large number of states, frequencies, and modalities. As such, measurement demands for antenna pattern characterization must accommodate a wide range of frequency bands, bandwidths [2], [3], and antenna form factors. Characterization becomes more difficult with devices operating at high frequencies and across large frequency bands, where measurement defects can lead to large errors in the estimated radiation pattern.

A standard approach for determining the radiation pattern of a device under test (DUT) is to apply a near-field to far-field transformation (NFT) on measurements of the DUT's near-field [4], [5], [6], [7], [8]. NFTs are particularly useful when far-field techniques impose costly measurement challenges [9], [10]. This is true, for example, of devices operating at millimeter wave frequencies (e.g., the FR2 band [2], [3]) where far-fields measurements suffer from path-loss issues. Near-field techniques can be done in a spatially compact measurement space and lead to the holographic [11], [12] ability to investigate the Fresnel ($0.62\sqrt{D^3/\lambda} \leq r \leq 2D^2/\lambda$, where r is the distance from the radiator, D is the diameter of the smallest sphere enclosing the radiator, and λ is the wavelength of the radiation) and Fraunhoffer ($2D^2/\lambda \leq r$) regions of antenna patterns. This is possible because NFTs extract the propagating spherical mode coefficients for the DUT's radiated field [13], which specify the DUT's radiated field in the near- and far-field. This ability is useful in array testing and in identifying defective array elements. Unfortunately, the measurements needed for the NFT-based approaches can take hours or days due to the high sample number dictated by typical sampling theorems [7], [8], [13], [14]. This becomes even more problematic when a device has multiple configurations that need to be characterized, as test equipment can drift away from proper operation over the course of many days/weeks.

In this work, we propose two techniques for broadband radiation pattern characterization by estimating the radiating mode coefficients of a DUT with minimal measurements. These methods modify standard NFT techniques with tools from compressed sensing (CS). Similar CS-based ideas have been used previously to reduce measurement requirements for radiation pattern characterization [7], [8], [14], [15], [16], [17], [18], [19]. In brief, CS helps reduce measurement requirements by leveraging structural assumptions about a DUT's Wigner D-function coefficients (WDFCs), which are estimated in the NFT process. Once the WDFCs are known, it is straightforward to derive the DUT's spherical mode coefficients, which define the near- and far-field radiation patterns or the DUT's sensitivity to

Manuscript received 14 December 2023; revised 24 April 2024 and 24 June 2024; accepted 27 June 2024. Date of publication 10 July 2024; date of current version 1 November 2024. This work was supported by NSF under Grant CCF–1704204 and Grant CCF–2106834 and in part by the US Department of Commerce Cooperative Agreement Award – Federal award ID number 70NANB23H025. Official contribution of the National Institute of Standards and Technology; not subject to copyright in the United States. The guest editor coordinating the review of this manuscript and approving it for publication was Dr. Kumar Vijay Mishra. *(Corresponding author: Marc Andrew Valdez.)*

Marc Andrew Valdez is with the Colorado School of Mines, Golden, CO 80401 USA, and also with the National Institute of Standards and Technology, Boulder, CO 80305 USA (e-mail: mvaldez@mines.edu).

Jacob D. Rezac and Joshua A. Gordon are with the National Institute of Standards and Technology, Boulder, CO 80305 USA (e-mail: jacob.rezac@nist.gov; josh.gordon@nist.gov).

Michael B. Wakin is with the Colorado School of Mines, Golden, CO 80401 USA (e-mail: mwakin@mines.edu).

This article has supplementary downloadable material available at https://doi.org/10.1109/JSTSP.2024.3424310, provided by the authors.

Digital Object Identifier 10.1109/JSTSP.2024.3424310

external radiation, and can be used for holographic projections within the near-field [11], [12]. These CS-based approaches are typically based on a sparse or compressible signal model (i.e., many WDFCs are zero or near zero).

The existing CS-based methods for NFTs are all designed for single-frequency operation. Research has been done outside of CS on broadband antenna characterization, e.g. [20], but such work relies on dense sampling grids. To perform the high-precision radiation pattern characterizations that are desirable for modern devices and required for broadband reference fields, existing CS methods would be applied one frequency at a time. The techniques we propose in this work leverage common structures across frequencies to further reduce measurement requirements. To do this, we model the broadband WDFCs with structure beyond single-frequency sparsity and compressibility in two ways: smoothness induced joint sparsity/compressibility across the desired characterization band and a low-dimensional matrix model where the DUT's WDFCs make up the columns of a low-rank matrix.

In this article, we compare the two proposed CS approaches and find both to be effective models for characterizing antenna radiation patterns with significant measurement number reductions. For the sparsity-based CS approach, we provide theoretical bounds on the approach's accuracy by leveraging the CS theory for bounded orthonormal systems (BOSs). For the low-rank CS approach, we provide an analysis of its limitations regarding theoretical guarantees in the context of the matrix sensing literature. Lastly, in numerical examples, we compare our proposed methods to existing CS methods for NFTs applied to broadband DUT characterizations and find significant reductions in measurement numbers and improved robustness to measurement noise.

The remainder of this article is arranged as follows. This section concludes with a summary of the paper's main problem, our solution approaches, and an overview of the existing related literature. Section II gives the necessary background on spherical NFTs and CS. Section III presents our theoretical results for CS in broadband NFTs. Section IV presents numerical examples pertaining to our approach for compressive broadband NFTs. Lastly, Section V provides our conclusions.

A. Notation

Throughout this paper we use the following notation. Uppercase bold math, e.g., $\boldsymbol{A}$, represents matrices, while lower case bold math, e.g., $\boldsymbol{a}$, represents vectors. A matrix or vector with * applied, e.g. $\boldsymbol{A}^*$ or $\boldsymbol{a}^*$, signifies the Hermitian adjoint. Similarly, ^{T} represents the transpose operation on a matrix or vector. An overline $\overline{x}$ represents the complex conjugate of x. Applied to a vector or function, $\|\cdot\|_p$ represents the typical ℓ_p or L_p norm, respectively, which should be clear from context. The symbol $\otimes$ signifies the Kronecker product. The inner product $\langle \boldsymbol{A}, \boldsymbol{B}\rangle_{HS}$ is the Hilbert-Schmidt inner product between matrices. We use the notation $\{x_i\}_{i=1}^N$ as shorthand for the set $\{x_i : i = 1, 2, \ldots, N\}$.

B. Problem Statement

In short, the goal of this article is to enable a spherical NFT for a DUT over a wide frequency band with as few measurements as possible. In Section II-A, we discuss how the spherical NFT problem for a single frequency reduces to finding a set of WDFCs for the DUT from a set of linear measurements of the DUT's near-field radiation. Once these are acquired, the transformation to the far-field radiation pattern is effectively a formality (thus, in our examples we will not compute this). In this light, our main problem is formally stated as follows:

Problem 1 (Primary Goal): Given a DUT and a set of N_f evenly spaced frequencies $\mathcal{F} = \{f_i\}_{i=1}^{N_f}$, let $\boldsymbol{a}_i \in \mathbb{C}^{N_D}$ be the vector of N_D WDFCs, indexed by m, μ, n, at the frequency f_i. That is, $[\boldsymbol{a}_i]_j = a_{n(j)}^{m(j)\mu(j)}(f_i)$ where $a_n^{m\mu}(f)$ are the frequency dependent WDFCs of the DUT associated with the Wigner D-functions $D_n^{\mu m}$. From as few spherical near-field measurements as possible (denoted by w, $\boldsymbol{w}$, $\boldsymbol{W}$, or $\boldsymbol{Y}$ depending on context), accurately recover $\boldsymbol{a}_i$ for all i.

C. Approach and Contributions

Problem 1 raises a few key questions to address in order to have a satisfactory solution approach: 1. What signal models can we impose to help estimate WDFCs? 2. What sampling patterns should be used? 3. How many measurements are needed? 4. What reconstruction algorithm should be used to estimate the WDFCs of a DUT from the measurements?

To answer questions 1–4, we propose two distinct types of approaches:

1) A sparse-model-based approach that can be treated as a BOS that incorporates both the spatial and frequency dependence of a DUT's radiation pattern while using monochromatic measurements.
2) A low-rank matrix reconstruction approach that can be used with either monochromatic or polychromatic measurements.

For the first type of approach, we prove two theorems about its accuracy when used to solve Problem 1 via basis pursuit (denoising), Theorems 8 and 9. For the second type of approach, no guarantee is available for the low-rank model.[1] However, we perform an extensive set of numerical experiments showing that the low-rank approach provides accurate WDFC reconstructions with high rates of compression and robustness to noise.

The sparsity-based approach we propose is novel in the CS and NFT literature. In particular, even though Theorem 8 is similar in flavor to other BOS results [18], [19], [21], [22], [23], using this model in the context of joint spatial and frequency NFT reconstructions is new. Moreover, Theorem 9, which is key to the effectiveness of the sparse-model-based approach, is entirely new; often there are no bounds on the sparse representation error of a particular physical signal in CS approaches, yet we arrive at an explicit bound in this article.

The low-rank matrix reconstruction approaches, while not novel in the broader CS literature, are novel in the NFT literature. To the authors' knowledge, no work has analyzed the effectiveness of low-rank approaches to accurately and efficiently reconstruct the WDFCs of a device. Moreover, no study of which

[1]The problems facing accuracy guarantees are discussed in the supplementary material.

we are aware has analyzed the additional benefit that polychromatic measurements can provide for compressive NFTs. Though polychromatic measurements are not seen in the literature, we include it as a possible driver of measurement system development—as we will see, it can provide improvements in accuracy using fewer samples than monochromatic samples, at least in some cases.

D. Prior Work

1) Sparse Signal Model: In spherical NFTs, CS using the sparsity model has been of keen interest to reduce measurement times in the *single* frequency context [7], [14], [16], [17], [18], [19]. In [14], [16], efforts were taken to establish experimental usefulness of sparsity/compressibility models applied to a DUT's single frequency WDFCs $\boldsymbol{a}_i$. Further development in [7], [8], [18] aimed to optimize sampling patterns and the number of samples versus reconstruction accuracy, again for single frequency WDFCs. These works, however, are either based on coherence, which is weak in terms of CS guarantees, or use experimental phase transition diagrams to infer the needed number of samples (often this is all that can be done when no guarantees are known). In contrast, [18] established theoretical guarantees based on the Restricted Isometry Property (RIP) for spherical NFTs and [19] extended RIP guarantees in spherical NFTs when realistic measurement restrictions are included. The former proved guarantees by considering the WDF series defined by a DUT in the context of the CS theory of BOS. The latter transformed the problem from WDFs to Slepian functions to create a BOS on a restricted measurement domain. Both of these works, however, require random samples on $\mathrm{SO}(3)$ (or a subdomain) and do not use the equiangular sample positions that are conventionally used [13]. An extension that allows for random subsamples of a measurement grid closer to conventional sample positions can be found in [23], which developed the Gauss-Legendre-quadrature-based sampling patterns used in this paper.

In summary, the prior sparsity-based work for spherical NFTs focused on sampling patterns and measurement reductions in the single frequency case. In principle, this work can be used to give a solution to Problem 1. However, such an approach would miss out on any joint structure to further improve sampling in the multi-frequency case. In contrast, to address questions 1-4 and thus Problem 1, we use the sparsity model to jointly solve for the WDFCs at *multiple* frequencies, i.e., all of the set $\{\boldsymbol{a}_i\}_{i=1}^{N_f}$. This sparsity model leverages smoothness properties present in the frequency dependence of a device's WDFCs and uses the same monochromatic measurements that existing single-frequency CS approaches use. We show that this model and solution approach can outperform the approach of solving for each $\boldsymbol{a}_i$ individually.

There has been additional work not discussed above to reconstruct broadband radiation patterns [24], [25], but these efforts are based on combinations of samples at different spatial positions using arrays of probes, which we do not consider. Moreover, these experiments do not incorporate theoretical details of the NFT measurements, i.e., their expansion in a known set of basis functions and the nature of the sparsity deriving from the coefficients in this basis.

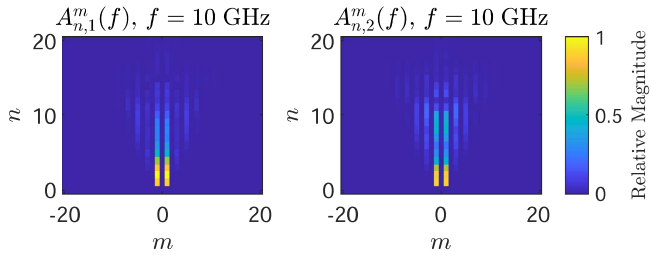

Fig. 1. *Horn Antenna VSWF Coefficients at 10 GHz.* The relative magnitude $|A^m_{n,\tau}|/\max_{n,m,\tau}|A^m_{n,\tau}|$ of the simulated VSWFCs $A^m_{n,\tau}$ from a simulated horn antenna at 10 GHz, in the middle of the device's operational band.

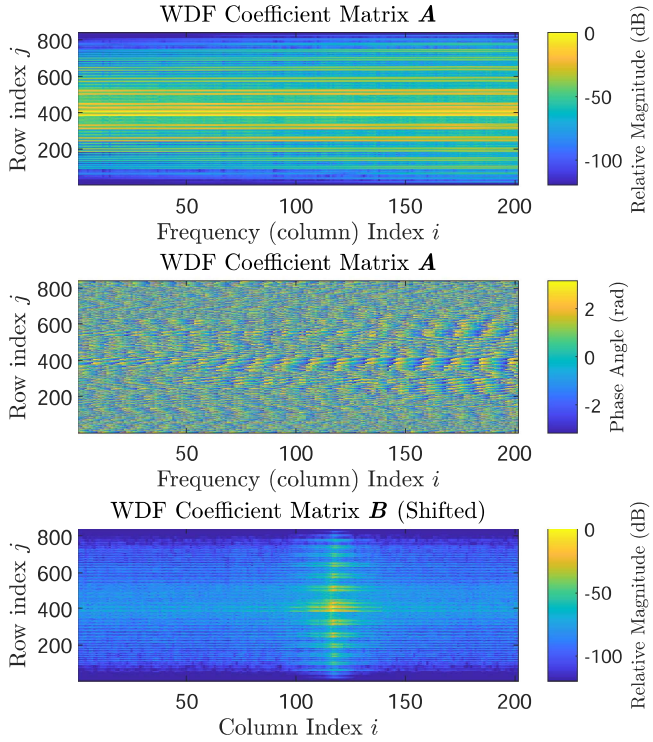

Fig. 2. *Horn Antenna WDF Coefficient Matrix.* The relative magnitude $|\boldsymbol{A}_{ij}|/\max_{i,j}|\boldsymbol{A}_{ij}|$ (top panel), absolute phase of $\boldsymbol{A}_{ij}$ (middle panel), and the relative magnitude $|\boldsymbol{B}_{ij}|/\max_{i,j}|\boldsymbol{B}_{ij}|$ of the Fourier transformed WDFC matrix $\boldsymbol{B}$ (bottom panel) for the simulated standard gain horn antenna using samples taken at 1 m using an x-directed electric dipole probe (a type of $\mu = \pm 1$ probe). The columns of $\boldsymbol{A}$ span the frequency band of 8–12 GHz with 201 samples, i.e., 20 MHz samples.

Additionally, we note that there are various other approaches to reconstruct multiple sparse vectors with common sparsity structures. Examples include multiple measurement vector (MMV) approaches and more [26], [27], [28], [29]. Many of these methods do not provide guarantees for structured measurements like BOSs, which is a primary goal of this article. Moreover, while there are guarantees in some MMV approaches, they are unsatisfactory for this work. In particular, MMV guarantees are only as good as single frequency CS in the most general case [29]. Lastly, many of these methods enforce row-sparse structure in the WDFCs $\boldsymbol{A}$. This structure is less than ideal

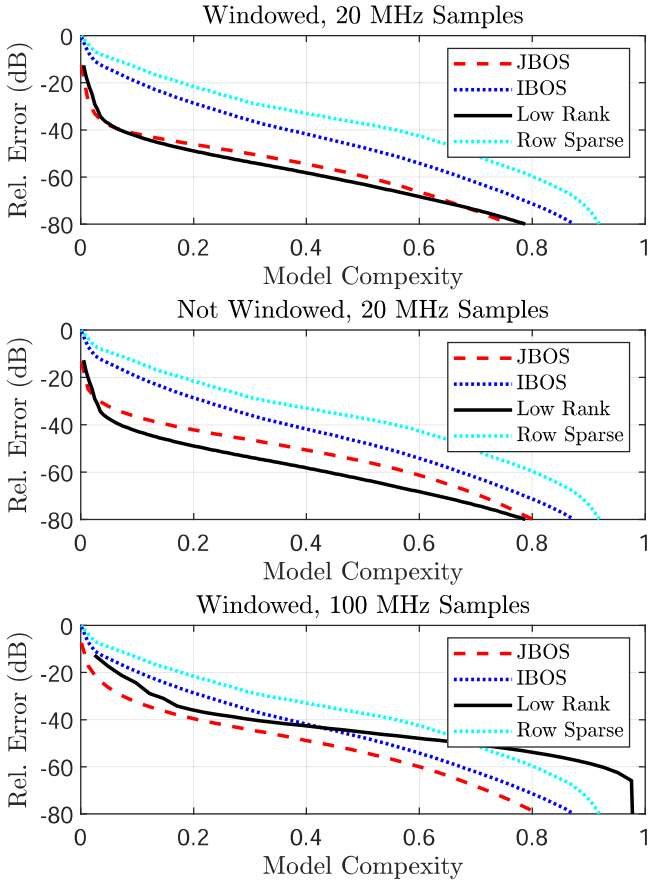

Fig. 3. *Model Representation Errors.* Sparse, low-rank, and row-sparse (MMV) model representation errors for the WDFCs of a simulated standard gain horn antenna as measured by a dipole probe from 8–12 GHz. Windowed results are windowed by a Planck-Taper window.

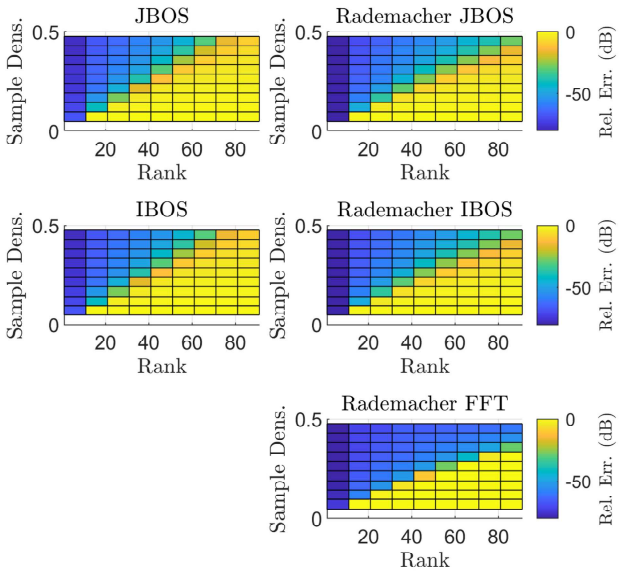

Fig. 4. *Noisy Low-rank Reconstruction PTD – Relative Error* The low-rank reconstruction phase diagrams the relative error of the solution in dB when samples are perturbed by additive noise. At each sample density and rank, we average over 50 trials.

NFTs because device WDFCs typically become more populated at higher frequencies. Thus, we expect more flexible models like our sparsity and low-rank ones to be more effective. Indeed, in basic tests, we see this effect for the MMV approach (see Fig. 3).

2) Low-Rank Signal Model: Rank awareness in matrix recovery problems has seen wide application and study. A broad overview of the subject is given in [30] while specific examples include hyperspectral imaging [31], [32], joint sparse recovery from ensemble signals or multi-sensor array signals [33], quantum state tomography [34], tensor recovery [35], [36], and more. However, to the best of our knowledge, there are no applications of rank-aware matrix sensing in the spherical NFT literature. We address this lack of study and present low-rank joint recovery approaches to which joint sparsity can be compared and while motivating further developments in the capabilities of spherical NFTs measurement systems. Here we note that some investigations have sought improved compressive sensing by combining sparse and low-rank models [37], [38]. These models utilize row-sparse matrices that are also low-rank. However, the restrictiveness of such signal models is unfavorable for NFTs (see the above discussion on simultaneously sparse signals). Thus, we do not combine sparse and low-rank models, though such an investigation may be an interesting avenue for future work if the inflexibility of combined spare and low-rank models can be removed in some manner.

A key underlying principle in these works is that the data of interest has a low-dimensional structure so that the matrix representation of the data is low-rank. We hypothesize that the WDFC matrix $\boldsymbol{A}$ for a DUT, in many cases, fits well into such a model. From an intuitive physical perspective, as the frequency of a DUT like a horn is changed, the radiation pattern does not change *too much* across its operational frequency. See, for example, the analytical expressions for horn antenna far-fields in [39]. Thus, its WDFCs should not vary too much, leading to the possibility that these changes can be described by a low dimensional model. Note, this behavior across a frequency band may not always be true; some devices gain side lobes in a non-smooth way, e.g., due to gratings. However, if the frequencies of such a critical change are known, one may still take advantage of smoothness on either side of such critical frequencies.

Beyond low dimensionality due to little change across frequency bands, the WDFCs being sparse at each frequency and, as we will see, compressible along frequency, imply there should be a low-dimensional representation of $\boldsymbol{A}$ that is at least equivalent to the savings we see in using the sparsity model.

II. Background

A. Spherical Near-Field to Far-Field Transformations

The spherical NFT has become a standard approach for characterizing the radiation pattern of a DUT (either receiving or transmitting). We will discuss the case where the DUT is transmitting and set up the spherical NFT in the single frequency case, which is standard. The receiving case can equally be handled by our methods; see [13] for details on the differences between the two cases.

The spherical NFT approach typically follows a standard set of steps. First, measurements are taken and expressed in terms of the DUT's radiated electric field using a known probe. The measurements are taken in the DUTs near-field on a sphere with radius r_{meas} enclosing and centered on the DUT. Since the measurements are taken using a probe, a process of probe correction must be used. This process relates the DUT's electric field to what the probe receives using rotation and translation transformations and then accounting for the probe's known field sensitivity [13]. The result of probe correction is that a measurement w is given by a linear combination of Wigner D-functions, $D_n^{\mu m}$ (defined formally below), whose coefficients are the DUT's WDFCs. The DUT's WDFCs are a product of the probes known sensitivity to fields and the DUT's vector spherical wavefunction coefficients (VSWFCs, also known as spherical mode coefficients), $A_{n,\tau}^m$, that define the DUT's radiated electric field. Using these near-field measurements, we construct and solve a linear inverse problem for the WDFCs, $a_n^{m\mu}$, from which we can get the VSWFs. We can then use these VSWFCs to project out in the radial direction to get the DUT's far-field or using holographic projections, investigate near-field regions. For conciseness, we do not carry out this procedure in our numerical examples; once the WDFCs are known, the DUT's far-field and holographic projections can be determined through known equations. Mathematically, the measurements are

$$w(\alpha,\beta,\gamma,f) = \sqrt{\sin\beta} \sum_{\tau,n,m,\mu} a_n^{m\mu}(f) D_n^{\mu m}(\alpha,\beta,\gamma), \quad (1)$$

where we use the shorthand $\sum_{\tau,n,m,\mu}$ to mean $\sum_{\tau=1}^{2} \sum_{n=0}^{n_{\max}} \sum_{m=-n}^{n} \sum_{\mu=-n}^{n}$. Here, $a_n^{m\mu}(f)$ are the WDFCs of the DUT. The WDFCs are a sum of the probe response constants [13] $C_{n,\tau}^{\mu}$ times the VSWFCs $A_{n,\tau}^m$ and the normalization constants $(c_n^{\mu m})^{-1}$ (see the definition of WDFs below):

$$a_n^{m\mu}(f) = \sum_{\tau=1}^{2} (c_n^{\mu m})^{-1} A_{n,\tau}^m(f) C_{n,\tau}^{\mu}(f). \quad (2)$$

The response constants contain the translation information of the spherical NFT as well as the probe's sensitivity to field modes, both of which stay constant (for a single radiating frequency) since r_{meas} is constant. In addition, the WDF arguments $(\alpha,\beta,\gamma) = (-\chi_{Euler}, -\theta_{Euler}, -\phi_{Euler})$, where $(\phi_{Euler}, \theta_{Euler}, \chi_{Euler})$ are Euler angles in the $zy'z''$ passive convention [40, p. 21] that specify the measurement position relative to the original DUT coordinate system.[2]

In the above formulation, the frequency dependence of the radiated field is contained only in the unknown WDFCs and the known probe response constants. We also note here the additional prefactor of $\sqrt{\sin\beta}$, which is not typical in most spherical NFTs literature. This prefactor is present because CS guarantees require it (see [18], [22], [41]). Practically speaking, the inclusion of the prefactor can be easily accounted for in spherical NFT implementations by computationally scaling measurements accordingly.

The WDFs described above form a basis for L_2 functions on the rotation group $\mathrm{SO}(3)$ [40] and are defined for $n \in \mathbb{N}_0,\ m,\mu \in \mathbb{Z},\ |m|,|\mu| \le n$ as

$$D_n^{\mu m}(\alpha,\beta,\gamma) = c_n^{\mu m} e^{-\mathrm{i}\mu\alpha} d_n^{\mu m}(\beta) e^{-\mathrm{i}m\gamma}, \quad (3)$$

where $c_n^{\mu m}$ is a normalization constant[3] and the Wigner d-function, $d_n^{\mu m}(\beta)$, is given by [40], [42]

$$\begin{aligned} d_n^{\mu m}(\beta) = {} & (-1)^{\mu-m}\sqrt{(2n+1)/2} \\ & \times \sqrt{(n+m)!(n-m)!(n+\mu)!(n-\mu)!} \\ & \times \sum_{\sigma=\max(0,m-\mu)}^{\min(n+m,n-\mu)} \xi_\sigma, \end{aligned}$$

$$\xi_\sigma = \frac{(-1)^\sigma \left(\cos\frac{\beta}{2}\right)^{2n-2\sigma+m-\mu} \left(\sin\frac{\beta}{2}\right)^{2\sigma-m+\mu}}{\sigma!(n+m-\sigma)!(n-\mu-\sigma)!(\mu-m+\sigma)!}. \quad (4)$$

Here, $(\alpha,\beta,\gamma) \in [0,2\pi) \times [0,\pi] \times [0,2\pi)$ parameterizes a point on $\mathrm{SO}(3)$. Later on, we will use the orthogonality relationship of WDFs,

$$\langle D_n^{\mu m} D_{n'}^{\mu' m'} \rangle \mathrm{SO}(3) = \int_{\mathrm{SO}(3)} D_n^{\mu m} \overline{D_{n'}^{\mu' m'}} \, \mathrm{dSO}(3) \quad (5)$$

$$= \frac{8\pi^2 (c_n^{\mu m})^2}{2n+1} \delta_{nn'} \delta_{mm'} \delta_{\mu\mu'}, \quad (6)$$

where $\mathrm{dSO}(3) = \sin\beta \mathrm{d}\alpha \mathrm{d}\beta \mathrm{d}\gamma$ For further details, see, e.g., [40] or [43].

B. Linear Inverse Problem Formulations

Given a set of measurements indexed by j at a fixed frequency f_i from Problem 1, i.e., $w(\alpha_j,\beta_j,\gamma_j,f_i)$, we can define the measurement vector $[\boldsymbol{w}_i]_j = w(\alpha_j,\beta_j,\gamma_j,f_i)$ and use (1) to form a fully determined linear inverse problem for the vector of WDFCs $\boldsymbol{a}_i$. Then, from the determined WDFs, we can straightforwardly find the VSWFCs using the known probe response constants. This single-frequency process is extended to fully determined versions of the multi-frequency linear inverse problems in (9) and (10), which we then describe compressive counterparts for in (11)–(14).

We can write the linear inverse problem for the single-frequency WDFs in matrix form as

$$\boldsymbol{w}_i = \boldsymbol{\Phi}_D \boldsymbol{a}_i + \boldsymbol{\eta}_i, \quad (7)$$

where $\boldsymbol{\eta}_i$ is a vector of noise associated with the measurements $\boldsymbol{w}_i$ and the entries of $\boldsymbol{\Phi}_D$, which we refer to as the measurement matrix, given by

$$[\boldsymbol{\Phi}_D]_{jl} = \sqrt{\sin\beta_j} D_{n(l)}^{\mu(l)m(l)}(\alpha_j,\beta_j,\gamma_j). \quad (8)$$

[2]The $zy'z''$ passive Euler angle convention is as follows: we first rotate the xyz coordinate system by ϕ_{Euler} about the z-axis into the $x'y'z'$-coordinate system; then we rotate from the $x'y'z'$-coordinate to the $x''y''z''$-coordinate by θ_{Euler} around the y'-axis; last we complete transformation by rotating the coordinate system by χ_{Euler} about the z''-axis.

[3]The definition of the WDFs with the arbitrary normalization constant is unconventional, but useful for our case. Depending on the use, e.g., for a continuous BOS, discrete BOS, or rotation operator for spherical wave functions, different values should be used. For a continuous BOS we use $c_n^{\mu m} = (\frac{2n+1}{8\pi^2})^{1/2}$, for a discrete BOS we use $c_n^{\mu m} = (C_g \frac{2n+1}{2})^{1/2}$ with C_g from [23, Th. 3 and Cor. 6], and for rotations of spherical wavefunctions we use $c_n^{\mu m} = 1$.

Here l indexes all possible values of the indices m, μ, n. If we now combine all frequencies in $\mathcal{F}$ using the same measurement positions $(\alpha_j, \beta_j, \gamma_j)$ we have the inverse problem

$$\boldsymbol{W} = \boldsymbol{\Phi}_D \boldsymbol{A} + \boldsymbol{H}, \tag{9}$$

where $\boldsymbol{W} = [\boldsymbol{w}_1\ \boldsymbol{w}_2 \cdots \boldsymbol{w}_{N_f}]$, with $\boldsymbol{A} = [\boldsymbol{a}_1\ \boldsymbol{a}_2\ \cdots\ \boldsymbol{a}_{N_f}]$ and $\boldsymbol{H} = [\boldsymbol{\eta}_1\ \boldsymbol{\eta}_2\ \cdots\ \boldsymbol{\eta}_{N_f}]$. As mentioned above, the spherical NFT measurements use only monochromatic radiation and (9) only requires monochromatic measurements.

In contrast to typical monochromatic NFTs and under the assumption that the propagation media has frequency-independent permeability and permittivity,[4] multiple frequencies could, in principle, be driven through the radiator and result in multi-frequency $a_n^{m\mu}(f)$, allowing us to set up a linear inverse problem of the form

$$\boldsymbol{Y} = \boldsymbol{\Phi}_D \boldsymbol{A} \boldsymbol{E} + \boldsymbol{H}, \tag{10}$$

where $\boldsymbol{E} = [\boldsymbol{\epsilon}_1\ \boldsymbol{\epsilon}_2\ \cdots\ \boldsymbol{\epsilon}_{N_\epsilon}]$, $N_\epsilon \geq N_f$, and the $\boldsymbol{\epsilon}_j \in \mathbb{C}^{N_f}$ define linear coefficients weighting linear combinations of the different radiated frequencies specified by $\boldsymbol{a}_i$. We will take the entries of each $\boldsymbol{\epsilon}_j$ to be i.i.d. Rademacher random variables. The purpose of choosing $\boldsymbol{E}$ this way is to provide an extra source of subgaussian randomness in sampling, which, heuristically, typically benefits CS methods [45]. Although any subgaussian distribution could be used here, we use Rademacher random variables to ensure that each single-frequency component of the broadband signal has the same magnitude. Other subgaussian distributions could result in arbitrarily large or small components. Combining radiated frequencies in this way is not usually done in spherical NFT applications due to limitations in the ability to accurately measure the phase of broadband signals in existing measurement systems. We hypothesize, though, that if measurements such as this were made possible in a new measurement apparatus,[5] it would improve the capability of compressive measurements for multi-frequency spherical NFTs.

Without any assumptions on the structure of the WDFCs, noiseless spherical NFTs require $(n_{\max}+1)(2n_{\max}+1)^2$ equiangular samples per frequency on SO(3) to make $\boldsymbol{\Phi}_D$ full column rank and have $\boldsymbol{A}$ be the unique solution to (9) and (10) when $\boldsymbol{H} = 0$ [13], [46]. However, it is common to use a probe that is only sensitive to the VSWFs $F_{n,\tau}^{\pm 1}$, called a $\mu = \pm 1$ probe, which reduces the sum over μ in (1) to only $\mu = \pm 1$ terms. This decreases the required number of samples to $N_{\text{sample}}^{\mu=\pm 1} := 2(n_{\max}+1)(2n_{\max}+1)$ per frequency. In a typical $\mu = \pm 1$ probe setup, the samples are equiangular on $[0, \pi]$ for θ_{Euler}, equiangular on $[0, 2\pi]$ for ϕ_{Euler}, and at $\chi_{Euler} \in \{0, \pi/2\}$ [13]. In contrast, we will not use equianglar sampling but instead consider the fully sampled and invertible spatial sampling pattern based on Gauss-Legendre quadrature [23], [46]. We use the Gauss-Legendre quadrature sampling pattern because it requires the same sample size to give a fully determined inverse problem, gives better CS guarantees than equiangular sampling, and still has fast sampling algorithms available [23].

1) Monochromatic Measurement Models: In the context of our goal to solve Problem 1, we will use two monochromatic compressive measurement models and two polychromatic compressive measurement models. Each of these models will be expressed as functions of the WDFCs via $\boldsymbol{A}$, or its Fourier transform. The monochromatic compressive models are subsamples of (9) expressed in terms of $\boldsymbol{A}$ or its Fourier transform $\boldsymbol{B} = \sqrt{N_f}^{-1} \boldsymbol{A} \boldsymbol{U}_F^*$, where $\boldsymbol{U}_F$ is the unitary DFT matrix. This means that $\boldsymbol{B}$ contains the DFT of the WDFCs $\boldsymbol{A}$ along the rows, i.e., across frequency f. This transform across f is independent of any sparsity or structure related to the Wigner D-functions. Moreover, the transformation does not have any effect on the measurements $\boldsymbol{W}$. Instead, the transform changes the basis in which we solve the inverse problem to enable compression in the frequency dependence of each individual Wigner D-function coefficient. This compression, as we will see in Section III, is due to DUT Wigner D-function coefficients varying smoothly with frequency.

The two monochromatic compressive measurement models we propose are (11) and (12)

$$P_\Omega\left(\text{vec}(\boldsymbol{W})\right) = P_\Omega\left(\left(\boldsymbol{I}_{N_f} \otimes \boldsymbol{\Phi}_D\right) \text{vec}(\boldsymbol{A}) + \text{vec}(\boldsymbol{H})\right), \tag{11}$$

$$P_\Omega\left(\text{vec}(\boldsymbol{W})\right) = P_\Omega\left(\sqrt{N_f}\left(\boldsymbol{U}_F^T \otimes \boldsymbol{\Phi}_D\right) \text{vec}(\boldsymbol{B}) + \text{vec}(\boldsymbol{H})\right), \tag{12}$$

where P_Ω selects a subset of the fully sampled measurements $\boldsymbol{W}$. Both of these compressive measurement models use direct subsamples of (9). We will call the form of the problem where the measurements are expressed as a function of $\boldsymbol{B}$ the joint BOS (JBOS). The case in (11), we will refer to as the individual BOS (IBOS). We name it IBOS because the measurement operator $\boldsymbol{I}_{N_f} \otimes \boldsymbol{\Phi}_D$ is block diagonal and each block is a BOS measurement matrix acting on the individual $\boldsymbol{a}_i$, i.e., each individual single frequency problem can be solved separately. In contrast, the JBOS formulation has a measurement matrix that is not block diagonal and is a BOS measurement matrix acting on all of the WDFCs jointly via $\text{vec}(\boldsymbol{B})$, which must be solved for all at once. As we will see in Section III-B, the form of the JBOS will be beneficial in recovering *all* $\boldsymbol{a}_i$ at once.

2) Polychromatic Measurement Models: As mentioned above, polychromatic measurements are not used in NFTs; however, we are including them in this paper's studies to investigate the potential benefit of such measurements in CS and propose a target capability for future measurement systems. For the compressive measurement model counterparts to the polychromatic problem (10), we consider (13) and (14),

$$P_\Omega\left(\text{vec}(\boldsymbol{Y})\right) = P_\Omega\left(\left(\boldsymbol{E}^T \otimes \boldsymbol{\Phi}_D\right) \text{vec}(\boldsymbol{A}) + \text{vec}(\boldsymbol{H})\right), \tag{13}$$

[4]This assumption is required so that the superposition principle holds, which then means that we can linearly combine single frequency radiation solutions to the Maxwell equations. Such an assumption will always hold in free space and will hold in air when the frequency band considered is not too wide compared to its center frequency [44]. In contrast, if the medium of propagation varies substantially with frequency, our models may not be applicable. When the superposition principle holds, any coefficients can be used for the superposition.

[5]We are not suggesting such measurements are currently possible, nor are we proposing a specific method to acquire these measurements. We are proposing a target capability for future measurement systems.

TABLE I
SPATIAL AND FREQUENCY SAMPLE POSITIONS FOR THE FOUR PROBLEM FORMULATIONS, IBOS, JBOS, RADEMACHER IBOS, RADEMACHER JBOS

Approach	Spatial Distribution	Frequency Distribution	Polychromatic	Frequency Combination Coefficients	Estimated Matrix
IBOS	GL Nodes	Equispaced	No	n/a	$\boldsymbol{A}$
JBOS	GL Nodes	Equispaced	No	n/a	$\boldsymbol{B}$
Rad. IBOS	GL Nodes	Equispaced	Yes	i.i.d. Rad.	$\boldsymbol{A}$
Rad. JBOS	GL Nodes	Equispaced	Yes	i.i.d. Rad.	$\boldsymbol{B}$

All use spatial sampling positions that are drawn from the gauss-legendre quadrature nodes. The main differences come from whether or not samples are monochromatic or polychromatic (i.e., frequencies linearly combined or not), indicated in the fourth column.

$$P_\Omega\left(\mathrm{vec}(\boldsymbol{Y})\right) = P_\Omega\left(\sqrt{N_f}\left(\boldsymbol{U}_F^T\boldsymbol{E}^T \otimes \boldsymbol{\Phi}_D\right)\mathrm{vec}(\boldsymbol{B}) + \mathrm{vec}(\boldsymbol{H})\right). \tag{14}$$

We call these the Rademacher IBOS and Rademacher JBOS sampling approaches, respectively.

We close this section with a table summarizing the above problem formulations. For each of the above approaches, Table I describes the spatial and frequency sample patterns and how they are combined into measurements.

C. Sparsity Model

The sparsity model has been widely used in the literature in a problem commonly referred to as compressed sensing (CS). In its simplest form, this problem is concerned with reconstructing an unknown vector $\boldsymbol{x} \in \mathbb{C}^N$ using a set of measurements $\boldsymbol{y} \in \mathbb{C}^M$, related by

$$\boldsymbol{y} = \boldsymbol{\Phi}\boldsymbol{x} + \boldsymbol{\eta}, \tag{15}$$

where $\boldsymbol{\Phi}$ is known as the measurement matrix and $\boldsymbol{\eta}$ is additive measurement noise. The CS model assumes that $\boldsymbol{x}$ is s-sparse (s nonzero entries) and $M < N$.

The pioneering work for this form of CS was done by Donoho, Candés, Romberg, and Tao [47], [48], [49], [50], which focus on random measurement matrices $\boldsymbol{\Phi}$. This work was soon followed by Rauhut [51] for structured $\boldsymbol{\Phi}$ such as those built from trigonometric polynomials. A comprehensive resource for CS can be found in [45].

A main focus of this initial work in CS was establishing algorithms and guarantees for solving (15) under the sparsity model. Though many algorithms are known, we will use quadratically constrained basis pursuit (basis pursuit denoising) [45, p. 85, $\mathrm{P}_{1,\eta}$] to solve (15) (and our corresponding inverse problems (11) and (12)),

$$\underset{\boldsymbol{z}\in\mathbb{C}^N}{\text{minimize}}\ \|\boldsymbol{z}\|_1 \quad \text{subject to } \|\boldsymbol{\Phi}\boldsymbol{z} - \boldsymbol{y}\|_2 \le \eta_0. \tag{16}$$

In QCBP, the goal is to find the sparsest vector that explains the observed measurements. The ℓ_1 norm is a convex relaxation of ℓ_0 and its minimization promotes sparsity [45], while the constraint ensures the solution is within the error explained by the additive measurement noise.

Letting the solution to (16) be an estimate of $\boldsymbol{x}$, which we denote by $\widehat{\boldsymbol{x}}$, guarantees about the accuracy of $\widehat{\boldsymbol{x}}$ have been formally studied in CS. In particular, it is known that $\boldsymbol{\Phi}$ satisfying the robust null space property [45, p. 86 Def. 4.17] is known to guarantee the accuracy of $\widehat{\boldsymbol{x}}$. It is well known that the robust null space property is difficult to prove directly for $\boldsymbol{\Phi}$, so a sufficient condition that implies that the (robust) null space property is the RIP. Note, when there is no measurement noise $\eta_0 = 0$ reduces (16) to basis pursuit and guarantees still apply.

Definition 1 (Restricted Isometry Property (RIP) [45, p. 133, Def. 6.1]): A matrix $\Phi \in \mathbb{C}^{M\times N}$ is said to satisfy the restricted isometry property of order s with constant $\delta \in (0,1)$ if for all s-sparse vectors $\boldsymbol{x} \in \mathbb{C}^N$

$$(1-\delta)\|\boldsymbol{x}\|_2^2 \le \|\Phi\boldsymbol{x}\|_2^2 \le (1+\delta)\|\boldsymbol{x}\|_2^2 \tag{17}$$

holds. The smallest δ, denoted by δ_s, is called the restricted isometry constant of order s.

The guarantee for the accuracy of $\widehat{\boldsymbol{x}}$ that relies on the RIP is given in [45, p. 144 Th. 6.12], which states that if $\boldsymbol{\Phi}$ satisfies the 2 s-RIP with small enough RIP constant, then the error between $\widehat{\boldsymbol{x}}$ and $\boldsymbol{x}$ is small for sparse or compressible $\boldsymbol{x}$. To measure the sparsity/compressibility of a vector in this context, we use the best s-sparse approximation error of $\boldsymbol{x}$.

Definition 2 (Best s-Sparse Approximation Error [45, p. 42, Def. 2.2]): Given a vector $\boldsymbol{x} \in \mathbb{C}^N$, the best s-sparse approximation error in the ℓ_p norm is

$$\sigma_s(\boldsymbol{x})_p = \min_{\boldsymbol{z}\in\mathbb{C}^N:\|\boldsymbol{z}\|_0\le s} \|\boldsymbol{z} - \boldsymbol{x}\|_p. \tag{18}$$

When the RIP-based conditions are satisfied, the accuracy of QCBP is bounded by the best s-sparse approximation error of $\boldsymbol{x}$ and the size of the measurement noise.

Theorem 3 (Accuracy of QCBP [45, p. 144 Th. 6.12]): If the measurement matrix $\boldsymbol{\Phi}$ satisfies the 2 s-RIP with

$$\delta_{2\,s} < 4/\sqrt{41}, \tag{19}$$

then, for any $\boldsymbol{x} \in \mathbb{C}^N$ and $\boldsymbol{y}$ such that $\|\boldsymbol{\Phi}\boldsymbol{x} - \boldsymbol{y}\|_2 \le \eta_0$, the solution of (16) satisfies

$$\|\boldsymbol{x} - \widehat{\boldsymbol{x}}\| \le Cs^{-1/2}\sigma_s(\boldsymbol{x})_1 + D\eta_0 \tag{20}$$

where $C, D > 0$ are constants that depend on $\delta_{2\,s}$.

Extensions and improvements in CS via RIP guarantees when $\boldsymbol{\Phi}$ is structured have been developed, in particular for sparse series expansions in different orthonormal bases [18], [19], [21], [22], [52], [53]. These results all establish a CS guarantee by proving a number of samples M needed to guarantee that the RIP is satisfied, at the core of which is the following result for BOSs.

Theorem 4 (RIP for Bounded Orthonormal Systems [45, p. 405, Th. 12.31]): Consider a set of basis functions $\phi_i : \mathcal{D} \to \mathbb{C},\ i \in \{1,2,\ldots,N\}$ that are orthonormal with respect to a probability measure ρ on the measurable space $\mathcal{D}$. Consider the matrix $\boldsymbol{\Phi} \in \mathbb{C}^{M\times N}$ with entries

$$[\boldsymbol{\Phi}]_{ji} = \phi_i(t_j),\ j \in \{1,2,\ldots,M\},\ i \in \{1,2,\ldots,N\} \tag{21}$$

constructed with i.i.d. samples of t_j from the measure ρ on $\mathcal{D}$. Suppose the orthonormal functions are bounded such that $\sup_{i\in\{1,\dots,N\}} \|\phi_i\|_\infty \leq K$. If

$$M \geq C_0 \delta^{-2} K^2 \, s \ln^4(N), \tag{22}$$

then with probability at least $1 - N^{-\ln^3(N)}$, the restricted isometry constant δ_s of $\frac{1}{\sqrt{M}}\boldsymbol{\Phi}$ satisfies $\delta_s \leq \delta$ for $\delta \in (0,1)$. The constant $C_0 \geq 0$ is universal.

D. Low-Rank Model

Similar to CS using a sparsity model, there are many approaches to recovering an unknown low-rank matrix $\boldsymbol{X} \in \mathbb{C}^{N\times P}$ from some number of linear measurements. In these approaches, measurements of are of the form

$$\boldsymbol{y} = \mathcal{L}(\boldsymbol{X}) + \boldsymbol{\eta} \tag{23}$$

where $\boldsymbol{y} \in \mathbb{C}^M$, $\mathcal{L}$ is a linear measurement operator $\mathcal{L}: \mathbb{C}^{N\times P} \to \mathbb{C}^M$ of the form

$$[\mathcal{L}(\boldsymbol{X})]_i = \langle \boldsymbol{X}, \boldsymbol{\Psi}_i \rangle_{HS}, \tag{24}$$

where $\langle \cdot,\cdot \rangle_{HS}$ is the Hilbert-Schmidt inner product, $\{\boldsymbol{\Psi}_i : \boldsymbol{\Psi}_i \in \mathbb{C}^{N\times P}, i = 1,2,\dots,M\}$ is a set of measurement matrices, and $\boldsymbol{\eta}$ is additive measurement noise.

In terms of reconstruction algorithms aimed at minimizing ℓ_2 distance between the samples $\boldsymbol{y}$ and $\widehat{\boldsymbol{y}}$ generated from a candidate solution $\widehat{\boldsymbol{X}}$, $\widehat{\boldsymbol{y}} = \mathcal{L}(\widehat{\boldsymbol{X}})$, one can consider iterative solvers subject to a low-rank constraint [30], [54]. Alternatively, similar to how sparsity-based CS minimizes the ℓ_1 norm to promote sparse solutions, we can minimize the nuclear norm (the sum of the singular values of a matrix) to promote low-rank solutions. This latter case is the equivalent of basis pursuit for low-rank matrices. In general, these low-rank reconstruction approaches can give guarantees similar to sparsity-based CS if the measurement operator $\mathcal{L}$ satisfies a matrix restricted isometry property (which we will refer to as M-RIP, not to be confused with the sparsity-based RIP) with small enough isometry constant.

Definition 5 (Matrix Restricted Isometry Property (M-RIP) [45, p. 133, Def. 6.1]): The measurement operator $\mathcal{L}: \mathbb{C}^{N\times P} \to \mathbb{C}^M$ is said to satisfy the matrix restricted isometry property of rank r with constant $\delta \in (0,1)$ if for all rank-r $\boldsymbol{X} \in \mathbb{C}^{N\times P}$

$$(1-\delta)\|\boldsymbol{X}\|_F^2 \leq \|\mathcal{L}(\boldsymbol{X})\|_2^2 \leq (1+\delta)\|\boldsymbol{X}\|_F^2, \tag{25}$$

holds. The smallest δ, denoted by δ_r, is called the matrix restricted isometry constant.

While guarantees for nuclear norm minimization are user friendly, the problem sizes we encounter in this paper make it desirable to solve (23) using methods based only on applications of our sampling operator and its adjoint (e.g., gradient descent). This is in contrast to many low-rank iterative methods for (23), which require repeated SVD calculations and are best for small to moderate sized problems. To that end, we instead will solve Problem 1 under the low-rank model using an approach that solves for the factors in $\boldsymbol{X} = \boldsymbol{U}\boldsymbol{V}^*$ using methods like gradient descent [55]. As an important note, the factors $\boldsymbol{U} \in \mathbb{C}^{N\times r}$ and $\boldsymbol{V} \in \mathbb{C}^{P\times r}$ are tall matrices, where the number of columns imposes a rank constraint.

In more detail, the work in [55] centers on solving a non-convex minimization problem for the Burer-Montiero (BM) factorization of $\boldsymbol{X}$, $\boldsymbol{X} = \boldsymbol{U}\boldsymbol{V}^*$, instead of solving a convex problem for $\boldsymbol{X}$. This alternative approach reduces computational complexity of the low-rank matrix recovery and, under certain assumptions (see [55, Th. 1, Remark 2]), has the property that any local minimizer of the non-convex problem is equivalent to the desired solution $\boldsymbol{X}$. In addition, satisfying the M-RIP with small enough isometry constant implies the BM factorized approach gives accurate results [55, Cor. 1]. Note, the measurement operator satisfying the M-RIP is not the only condition to imply this result for the BM factorized approach. The M-RIP implies restricted strong convexity and smoothness, which is the key property needed in [55]. As applied to our low-rank matrix sensing problem, the BM factorized approach solves the minimization problem,

$$\underset{\boldsymbol{U}\in\mathbb{C}^{N\times r}, \boldsymbol{V}\in\mathbb{C}^{P\times r}}{\text{minimize}} \; \frac{1}{2}\left\|\boldsymbol{y} - \mathcal{L}\left(\boldsymbol{U}\boldsymbol{V}^*\right)\right\|_2^2. \tag{26}$$

In the context of matrix sensing as described above, we can recast the IBOS, JBOS, Rademacher IBOS, and Rademacher JBOS sampling operators to match the standard notation used in the literature:

$$[\mathcal{L}_{IBOS}(\boldsymbol{A})]_k = \left\langle \boldsymbol{A}, \overline{\boldsymbol{\phi}_{D,i(k)}} \boldsymbol{e}_{j(k)}^* \right\rangle_{HS} \tag{27}$$

$$[\mathcal{L}_{Rad.\,IBOS}(\boldsymbol{A})]_k = \left\langle \boldsymbol{A}, \overline{\boldsymbol{\phi}_{D,i(k)}} \boldsymbol{\epsilon}_{j(k)}^* \right\rangle_{HS} \tag{28}$$

$$[\mathcal{L}_{JBOS}(\boldsymbol{B})]_k = \sqrt{N_f}\left\langle \boldsymbol{B}, \overline{\boldsymbol{\phi}_{D,i(k)}} \boldsymbol{e}_{j(k)}^* \boldsymbol{U}_F^* \right\rangle_{HS} \tag{29}$$

$$[\mathcal{L}_{Rad.\,JBOS}(\boldsymbol{B})]_k = \sqrt{N_f}\left\langle \boldsymbol{B}, \overline{\boldsymbol{\phi}_{D,i(k)}} \boldsymbol{\epsilon}_{j(k)}^* \boldsymbol{U}_F^* \right\rangle_{HS} \tag{30}$$

where $\boldsymbol{\phi}_{D,i(k)}^T$ is a row selected at random from the BOS measurement matrix $\boldsymbol{\Phi}_D$, $\boldsymbol{e}_{j(k)}^*$ is a randomly selected standard basis vector, $\boldsymbol{\epsilon}_i^*$ is a random vector whose entries are i.i.d. Rademacher random variables, and $\boldsymbol{B}$ is defined as above in Section II-C. Note, (11)–(14) use the same samples as (27)–(30), respectively. See Supplementary Material Section VII for details.

III. Theoretical Analysis

In this section, we outline the theoretical guarantees (or lack thereof) for Problem 1 under the sparsity and low-rank models.

A. Individual BOS

The treatment of (7) using the sparsity model has been well studied in the individual frequency case. The following theorem establishes a BOS-based guarantee for the IBOS sampling approach when we assume a total budget of M measurements to be used across all frequencies.

Theorem 6 (IBOS Estimation of Wigner D-function Coefficients): Consider Problem 1 and assume a budget of M measurements are spread evenly across all frequencies such that at each frequency we take at least $\lfloor M/N_f \rfloor \geq C' N_D^{1/6} s_{IBOS} \ln^4(N_D)$ measurements drawn i.i.d. from the

appropriate distribution [23, Th. 3 and Cor. 6], where C' is a constant and s_{IBOS} is a positive integer. Moreover, assume the measurement noise for each frequency satisfies $\|\boldsymbol{\eta}_f\|_\infty \leq \eta_0$ and that we use these measurements to estimate the WDFCs for each frequency individually using (16) to solve the inverse problem (11) normalized as a discrete BOS [23, Th. 3 and Cor. 6] (i.e., we are solving the single-frequency problems $\boldsymbol{w}_i = P_{\Omega'}\boldsymbol{\Phi}_D\boldsymbol{a}_i + \boldsymbol{\eta}_i$ for each i individually using QCBP). Then with probability least $1 - N_D^{-\ln^3(N_D)}$, the individual estimated WDFCs, $\widehat{\boldsymbol{a}}_i$, satisfy

$$\|\boldsymbol{a}_i - \widehat{\boldsymbol{a}}_i\|_2 \leq \frac{C}{\sqrt{s_{IBOS}}}\sigma_{s_{IBOS}}(\boldsymbol{a}_i)_1 + D\eta_0, \tag{31}$$

where $C, D > 0$ are universal constants. Moreover, the matrix of estimated WDFCs, $\widehat{\boldsymbol{A}} = [\widehat{\boldsymbol{a}}_1\ \widehat{\boldsymbol{a}}_2\ \cdots\ \widehat{\boldsymbol{a}}_{N_f}]$ satisfies, with probability at least $1 - N_f N_D^{-\ln^3(N_D)}$,

$$\left\|\boldsymbol{A} - \widehat{\boldsymbol{A}}\right\|_F \leq \frac{C}{\sqrt{s_{IBOS}}}\sum_{i=1}^{N_f}\sigma_{s_{IBOS}}(\boldsymbol{a}_i)_1 + DN_f\eta_0. \tag{32}$$

Proof: See Supplementary Material Section VI.

Remark 7: A notable fact about (32) is that the term in the error due to measurement noise is not affected by increases in the measurement number, M, and it increases if the number of frequency samples, N_f, increases. The former attribute is fundamentally due to the structure of QCBP. The QCBP problem has the quadratic constraint grow with each measurement used and so the accuracy limit depends on the assumed maximum error in any given measurement.

B. A Joint BOS for Broadband NFTs

Due to the tensor product nature of the measurement operator (12), this measurement operator fits the criteria to be a BOS for the vector $\text{vec}(\boldsymbol{B})$. In particular, this operator is a BOS sampling operator if the subsampling operator P_Ω is defined so that a given measurement has a spatial position selected according to the BOS distribution for $\boldsymbol{\Phi}_D$ specified in [23, Th. 3 and Cor. 6] and the frequency for the measurement (i.e., the row of $\boldsymbol{U}_F^T$) is selected at random independently of the position. Additionally, the bound on the magnitude of the entries of the JBOS operator is the same as $\boldsymbol{\Phi}_D$, since the scaled DFT matrix $\sqrt{N_f}\boldsymbol{U}_F$ has all entries of magnitude one. Pairing these facts we can apply BOS guarantees under the sparsity model to (11).

Theorem 8 (JBOS Estimation of Wigner D-function Coefficients): Consider the linear inverse problem specified by (12), normalized so that the WDFs are a discrete BOS, with measurement noise bounded so that $\|\boldsymbol{\eta}_i\|_\infty \leq \eta_0, \forall i$. Suppose $M \geq C' N_D^{1/6} s_{JBOS} \ln^4(N_D N_f)$ samples are taken i.i.d. from the product distribution having a uniform distribution on the rows of $\boldsymbol{U}_F^T$ and the spatial portion, the rows of $\boldsymbol{\Phi}_D$, are distributed according to the BOS distribution specified in [23, Th. 3 and Cor. 6]. Let (16) provide an estimate $\text{vec}(\widehat{\boldsymbol{B}})$ of the coefficients $\boldsymbol{B} = \sqrt{N_f}^{-1}\boldsymbol{A}\boldsymbol{U}_F^*$ and the estimated WDFC matrix be $\widehat{\boldsymbol{A}} = \sqrt{N_f}\widehat{\boldsymbol{B}}\boldsymbol{U}_F$. Then, with probability at least $1 - (N_f N_D)^{-\ln^3(N_f N_D)}$, $\widehat{\boldsymbol{A}}$ satisfies

$$\left\|\boldsymbol{A} - \widehat{\boldsymbol{A}}\right\|_F \leq C\sqrt{\frac{N_f}{s_{JBOS}}}\sigma_{s_{JBOS}}(\text{vec}(\boldsymbol{B}))_1 + D\sqrt{N_f}\eta_0, \tag{33}$$

where $C, D > 0$ are constants depending on the restricted isometry constant $\delta_{2s_{JBOS}}$ of $\sqrt{N_f}P_\Omega\boldsymbol{U}_F^T \otimes \boldsymbol{\Phi}_D$.

Proof: See Supplementary Material Section VI.

Comparing the error results in Theorems 6 and 8, the noise term of the IBOS approach grows faster by a factor of $\sqrt{N_f}$ in Theorem 6. In terms of the sparse representation error term, the picture is a bit less clear. In later numerical examples, we will see that the sparse representation error for the JBOS is much more controlled, especially as N_f increases. However, this does not justify, theoretically, why we might expect the JBOS to perform better with respect to sparse representation error.

To that end, we analyze the sparse representation error in the JBOS case assuming the WDFCs are infinitely differentiable with respect to frequency. Using this assumption and properties of Fourier series expansions, we bound the sparse representation error of $\boldsymbol{B}$.

Theorem 9: Let $\boldsymbol{B} = \sqrt{N_f}^{-1}\boldsymbol{A}\boldsymbol{U}_F^*$ be the matrix of JBOS coefficients for a DUT with WDFC matrix $\boldsymbol{A}$ whose frequency samples are specified by Problem 1 and N_f is even (similar statements can be made for odd N_f). Assume the maximum sparsity of any column of $\boldsymbol{A}$ is $s_{\max}$ and each other column has a support contained in the support of this $s_{\max}$-sparse column. Moreover, assume the WDFCs are scaled by a windowing function so that the periodization of the WDFCs,

$$a_n^{m\mu}(\zeta) = a_n^{m\mu}\left(f_1 + \zeta\frac{\Delta_f + \delta_f}{2\pi} + \frac{\Delta_f + \delta_f}{2}\right) \tag{34}$$

where $\zeta \in [-\pi, \pi]$, $\Delta_f = f_{N_f} - f_1$, and $\delta_f = f_{i+1} - f_i$, is infinitely differentiable with respect to ζ (frequency). Then, for positive integer j, the sparse representation error of $\boldsymbol{B}$ satisfies, $\forall p > 2$,

$$\sigma_{(2j+1)s_{\max}}(\text{vec}(\boldsymbol{B}))_1 \leq \frac{\kappa'(p)N_f N_D^{1/2} s_{\max}}{j^{p-2}} \tag{35}$$

$$\leq \frac{\kappa'(p)N_f N_D^{3/2}}{j^{p-2}}, \tag{36}$$

where $\kappa'(p)$ is a constant depending on p and the p-th derivatives of the WDFCs.

Proof: See Supplementary Material Section VI.

The assumption regarding the maximum column sparsity and support is quite restrictive, but for many standard radiators this pattern is seen to hold, e.g., the horn antenna WDFCs in Fig. 2. Moreover, the form of (35) is rather complicated but can be thought of in the following way: If each WDFC has a sparsity $s_{\max}$ or less, and we sample at a positive integer multiple j of $s_{\max}$ (times the factors from Theorem 8), then the error has superpolynomial decay in this multiple j. Additionally, we actually expect this bound to be loose in cases of devices like horn antennas. This is because the explicit matrix we construct to bound the sparse representation error in our proof is constrained to fill each row with equally many entries. This could mean that

the matrix we use is not a good sparse approximation to $\boldsymbol{B}$. This is because it is possible, and seemingly likely for certain devices (see Theorem 8), that certain rows of $\boldsymbol{B}$ contain multiple entries larger than any entry in another row.

We can now compare Theorem 8 with Theorem 6 in the context of Theorem 9. Take the assumptions needed for Theorem 9 and also assume we take a total of $C' q s_{\max} N_D^{1/6} \times (log\ factors)$ noiseless samples (noting the difference in log factors between Theorems 6 and 8), where $q > 0$ is an integer. According to Theorem 6, one would expect to recover the $qs_{\max}/N_f$ largest entries of each WDFC vector $\boldsymbol{a}_i$. As we increase q, we recover the next largest entries in each WDFC vector. However, we *do not know* how the error of the Theorem 6 estimate decays because we do not know how the magnitude of the WDFC vectors' entries decay. In contrast, using Theorem 8 and Section II-C, as we increase q *we do know* how the error decays. This error decays superpolynomially with q, thanks to the smoothness properties of the WDFCs with respect to frequency.

Regarding the assumption of smooth WDFCs used above, this property will hold so long as the VSWFCs for the DUT and the probe sensitivity are also infinitely differentiable with respect to frequency, which will be valid in free space and other simple propagation media.[6] This is due to the form of the translation operator only depending on frequency in the spherical Hankel functions, which are continuously differentiable with respect to frequency. We note that other research has also relied on similar frequency smoothness assumptions for antennas [20]. Moreover, for dipole probes and common DUTs like horn or aperture antennas, infinite differentiability is a reasonable assumption based on theoretical analyses in [13], [39].

C. Low-Rank Approaches

In Section III-A and III-B, we saw that the theoretical RIP guarantees from the CS literature are readily applied to the sparsity based approaches for Problem 1. In contrast, M-RIP results from the theory of low-rank matrix sensing are not readily applied to Problem 1. This inability is due to the structure of the BOS sensing operators in (27) and (29) (similarly the operators in (28) and (30)); the structure is problematic because various existing results either do not directly apply or their existing proof approaches, e.g., in [34], [35], [45], [56], do not permit translation to the BOS sampling operators structure. We discuss this topic in more detail in the Supplementary Material (see Section VIII).

IV. Numerical Experiments

In this section, we examine the effectiveness of sparsity and low-rank models. First, in Section IV-A, we discuss some general computational considerations when using either model—even for relatively small band-limits, $n_{\max}$, problem sizes can become large when used for a typical horn antenna. In Section IV-B, we examine the effectiveness of the sparsity and low-rank models for a typical horn antenna. Section IV-C analyzes the success of using the sampling operators defined in Section II-D, as we do not have theoretical guarantees like we do for the sparsity model. Lastly, in Section IV-D, we compare the reconstruction results for the sparsity and low-rank models.

A. Computational Considerations and Fast Algorithms

Applying the sampling operator or its adjoint/inverse in NFT algorithms can become difficult, even in the single frequency case. This fact is due to the scaling in the problem size with the band limit, either $n_{\max}^2$ in the $\mu = \pm 1$ probe case or $n_{\max}^3$ more generally. Thus, fast NFT algorithms are highly important for NFTs over a large frequency range. In the fully sampled NFT, it is possible to implement a fast approach using FFTs [13]. However, to have guaranteed CS with fast NFTs, more work is required.

For CS guarantees to apply to sub-sampled NFTs, the first guarantees required continuous random sampling on $\mathrm{SO}(3)$ or a subset of $\mathrm{SO}(3)$ [18], [19]. Such continuous random sampling renders existing fast algorithms unusable. A modest improvement in the situation is found in [57]; however, the scaling of the guarantees is worse than the continuous counterpart. Fortunately, CS guarantees of the same scaling as the continuous sampling can be extended to sampling positions amenable to a fast algorithm [23]. This approach allows sampling on the Gauss-Legendre nodes for the polar angle β in the WDFs, enabling the use of the fast algorithm in [46]. Thus, in our numerical examples, we use the algorithm in [46] for the WDF transform and its adjoint, paired with FFTs/IFFTs for the frequency dependence of the WDFCs. Table II compares the fully-sampled computation time and memory complexity of the forward (or adjoint/inverse) sampling operator using the fast algorithm [46] with the full matrix approach used for continuous random sampling on $\mathrm{SO}(3)$. It is worth commenting that, even though we formulate our problem using Kronecker products in (11) and (12), the computational complexities are identical to computing $\boldsymbol{\Phi}_D \boldsymbol{A}$ and $\boldsymbol{\Phi}_D \boldsymbol{B} \boldsymbol{U}_F$. Note also that the Rademacher counterparts will fare worse computationally due to the need to fully compute the matrix products containing $\boldsymbol{E}$ from (10).

B. Model Efficiency

Both the sparse and low-rank models we propose should, if they are useful models, provide a significant level of compression that we can leverage in the sensing for Problem 1. The level of compression of a signal under such models generally translates to sampling savings, at least in an idealized scenario. For example, if a BOS has the optimal bound ($K = 1$), then, up to logarithmic factors, the number of samples needed to represent an s-sparse signal is proportional to s. A similar case is true when using M-RIP guarantees and nuclear norm minimization or using or BM factorized matrix sensing as described in Section II-D. Thus, to get an idea of the effectiveness of each model, we look at the relative error when representing the WDFCs of a simulated

[6] Complicated media where permeability and permittivity do not vary smoothly with frequency will be problematic and lessen the effectiveness of the DFT across frequency since they will affect the smoothness properties of the WDFCs.

TABLE II
COMPUTATIONAL COMPLEXITY AND MEMORY COMPLEXITY OF DIFFERENT SAMPLING OPERATOR IMPLEMENTATIONS FOR NFTS (NO ASSUMPTIONS ON PROBE)

Approach	Complexity (Single-Frequency)	Memory (Single-Frequency)	Complexity (Multi-Frequency)	Memory (Multi-Frequency)
Matrix	$O(n_{\max}^6)$	$O(n_{\max}^6)$	$O(n_{\max}^6 N_f^2)$	$O(n_{\max}^6 N_f^2)$
Fast	$O(n_{\max}^4)$	$O(n_{\max}^3)$	$O(n_{\max}^4 N_f \log N_f)$	$O(n_{\max}^3)$

The matrix row is the full matrix approach that would be used with continuous samples on so (3) while the fast algorithm [46] is enabled by sampling on gauss-legendre nodes.

standard gain horn antenna using the best sparse or low-rank approximation of a given model complexity. The relative error is defined as

$$\text{Relative Error (dB)} = 20\log_{10}\left(\left\|\boldsymbol{A}-\widehat{\boldsymbol{A}}\right\|_F / \|\boldsymbol{A}\|_F\right) \quad (37)$$

where $\widehat{\boldsymbol{A}}$ is the best s-sparse approximation to $\boldsymbol{A}$ under the JBOS or IBOS assumptions, or the best rank-r approximation of $\boldsymbol{A}$. For the JBOS this means $\widehat{\boldsymbol{A}} = \sqrt{N_f}\widehat{\boldsymbol{B}}\boldsymbol{U}_F$ and $\widehat{\boldsymbol{B}}$ contains the s largest magnitude entries of $\boldsymbol{B}$, while for the IBOS, this means each column $\widehat{\boldsymbol{A}}$ contains the best $\lfloor s/N_f \rfloor$-sparse approximation to the corresponding column in $\boldsymbol{A}$. This selection is made for the IBOS as it represents a model with a budget of s entries to keep and we do not know which columns of $\boldsymbol{A}$ are larger in general. We define model complexity as

$$\text{Model Complexity} = \begin{cases} \frac{s}{N_D^{\mu=\pm1} N_f}, & \text{for an } s\text{-sparse model} \\ \frac{r}{\min(N_D^{\mu=\pm1}, N_f)}, & \text{for a rank-}r\text{ model} \end{cases}. \quad (38)$$

where $N_D^{\mu=\pm1}$ is the dimension of the WDF basis restricted to only the $\mu = \pm1$ WDFs since we assume a $\mu = \pm1$ probe. For the sake of comparison, we will also include the best row-sparse approximation to $\boldsymbol{A}$, which is the matrix we would recover using the MMV approach mentioned in the introduction [26], [27].

Below, we consider VSWFCs standard gain horn antenna, with an approximate operational band of 8–12 GHz, described in [39, Fig. 13.22]. The VSWFCs for this horn are generated as follows. We use the MATLAB Antenna Toolbox[7] `horn` object to specify a horn antenna using the specifications in [39, Fig. 13.22], set the waveguide feeding the horn to match the width and height of WR90 waveguide, and tilt the horn using `"Tilt", [-90 90]`, with `"TiltAxis", [0 1 0; 0 0 1]`. The tilting procedure orients the horn to have its main lobe along the z-axis. The remainder of the parameters for the `horn` method are left at their defaults. We then use the function `EHfields` to simulate the electric field for the horn antenna in the near-field on a sphere of radius 1 m centered on the point $(x, y, z) = (0, 0.5 * \texttt{horn.Height}, 0.1)$. For the dimensions of the antenna and frequencies we consider, this puts the Fresnel region defined by $0.62\sqrt{D^3/\lambda} \leq r \leq 2D^2/\lambda$ at roughly 0.3 m to 4–5 m. Here, D is the diameter of the smallest sphere circumscribing the radiator and λ is the wavelength of the radiation. We then extract the VSWFCs using the angular orthogonality of the VSWFs (see [13, Appendix A1.4.3]). The VSWF coordinate system is aligned parallel with the horn's but centered on the center of the sphere for which the electric field is known. We shift the sphere and use its center for the coordinate system of the VSWFs to better center the horn antenna with the origin of the VSWFs and provide better VSWFC compressibility. For computational simplicity, we set the band-limit of the VSWF expansion for the field to $n_{\max} = 20$, which gives reasonably accurate field representations (the typical $n_{\max} = kr + 10$ rule gives $n_{\max} \approx 25$). Example VSWFCs for the horn antenna at 10 GHz can be seen in Fig. 1.

When investigating measurements w, we simulate these in-computer according to (1) and (2) by using the VSWFCs and assuming samples are taken at a radius of 1 m using an x-oriented dipole probe (probe response constants are in [13, Eqs. 3.39 and 3.40]). This radius puts the measurements well within the Fresnel region referenced above. Using the dipole probe, only the WDFCs with $\mu = \pm1$ are nonzero, so $\boldsymbol{A}$ is $N_D^{\mu=\pm1} \times N_f$. In Fig. 2, we show the relative magnitude and absolute phases of the entries of $\boldsymbol{A}$ as well as the relative magnitude of the transformed coefficient matrix $\boldsymbol{B}$. Both $\boldsymbol{A}$ and $\boldsymbol{B}$ can be seen to be sparse/compressible, with the transformation applied to get $\boldsymbol{B}$ resulting in increased sparsity/compressibility.

As a note, an analysis of the theoretical far-field of the horn we consider [39, Eqs. 13-46(a-c)] (omitted for the sake of brevity) shows WDFCs that are much more sparse than Fig. 2—the large coefficients are similar in structure, but the tail of smaller coefficients on $\boldsymbol{A}$ are more towards -100 dB to -120 dB versus the -40 dB to -60 dB range we see in Fig. 2. We hypothesize the difference between such an analysis and Fig. 2 is in part due to the mesh sizes used in the method of moments method MATLAB uses for field calculations and to simplifying assumptions used to arrive at [39, Eqs. 13-46(a-c)]. However, real horn antennas will likely also be more akin to Fig. 2, due to small imperfections as well as the fact that the analysis in [39] is quite simplified.

As a further note, devices with wider operational bands than our example do exist. However, as long as the field varies smoothly with frequency in the operational band as our example does, we do not expect the analysis of such devices to differ significantly.

In Fig. 3, we see that each model provides compression when used with different frequency sample densities and with or without windowing included. Using a Planck-Taper window (i.e., smoothing out the edges of the DFT across frequency) and a frequency sampling of 20 MHz, both the JBOS and the low-rank models achieve an accuracy of around -40 dB at a model complexity of near 0.1. In contrast, the IBOS model does not reach comparable accuracy until the model complexity is much larger, near 0.4. The MMV approach fares even worse

[7]Commercial software is identified in this paper in order to specify the experimental procedure adequately. Such identification is not intended to imply recommendation or endorsement by the National Institute of Standards and Technology, nor is it intended to imply that the materials or equipment identified are necessarily the best available for the purpose.

than the IBOS under the same conditions. This result is primarily due to the fact that the compression is done by removing rows of $\boldsymbol{A}$, not just individual entries like the JBOS or IBOS methods.

The results we see in Fig. 3 are promising for using any of the proposed models for CS of all coefficients in $\boldsymbol{A}$, but the actual effectiveness of the sensing will heavily depend on the reconstruction approach and how close to optimal it comes (here optimal is meant in the sense of needed number of samples for a given model complexity).

Looking more critically at Fig. 3, the number of frequency samples in the given band has a large effect on the low-rank and JBOS models. Comparing the top panel to the bottom panel (both of which window the same ranges from 8–8.3 GHz and 11.7–12 GHz), a change in frequency sample density from 20 MHz to 100 MHz significantly affects the low-rank model and has a slight effect on the JBOS model, but little effect is seen in the IBOS or row-sparse MMV model. Comparing the top and middle panel, we can see the windowing significantly affects the JBOS model for the better, but it has little effect on the low-rank or IBOS models.

C. General Low-Rank Reconstruction Phase Diagrams

It is common in the CS literature to demonstrate the general effectiveness of a reconstruction approach by using a phase transition diagram (PTD) that plots reconstruction accuracy versus sampling rate and signal model complexity (i.e., sparsity level or matrix rank). Since we have no theoretical guarantees for our low-rank reconstruction approaches, we give phase transition diagrams for each approach using noisy samples Fig. 4. In this figure, each sample has noise drawn uniformly at random from the complex disk with radius r_{noise} where $peak\ signal/r_{noise} =$ 70 dB. For noiseless samples see Supplementary Material Section IX.

To generate the phase transition diagrams, we run 50 trials at each displayed rank and sample density,

$$\text{Sample Density} = \#\text{ of samples}/\left(N_{\text{sample}}^{\mu=\pm1} N_f\right) \tag{39}$$

where $N_{\text{sample}}^{\mu\pm1} := 2(n_{\max}+1)(2n_{\max}+1)$ is the number of measurements in fully sampled NFTs at an individual frequency, and we have set $n_{\max} = 10$ and $N_f = 200$. Note that $N_{\text{sample}}^{\mu=\pm1}$ is roughly double $N_D^{\mu\pm1}$, owing to the form of the orthogonality relationship for Wigner D-functions and associated sampling theorems [13], [46]. In each trial we use 26 to reconstruct a unit Frobenius norm matrix $\boldsymbol{X} \in \mathbb{C}^{N_D^{\mu=\pm1} \times N_f}$ from its measurements. We generate a rank r matrix $\boldsymbol{X}$ by selecting the r singular values uniformly at random from [0.01,1] (selected to avoid extremely poor conditioned matrices). The singular vectors are selected uniformly at random from the Haar measure on unitary matrices [58]. To solve (26) we use gradient descent with a maximum of 250 iterations and fix the rank estimate as the known rank r. The random samples for the IBOS and JBOS model are selected according to their BOS distribution described in [23]. For their Rademacher counterparts, the spatial samples are distributed the same as the non-Rademacher operators and at each measured spatial point a new coefficient vector $\boldsymbol{\epsilon}$ is generated. To initialize the gradient descent algorithm in the IBOS and JBOS cases, we use the inverse operators of the full IBOS and JBOS operators applied to the random subsamples. These inverse operators use the inverse operator in [46] (paired with an extra DFT in the JBOS case). For the Rademacher IBOS and JBOS sampling operators, since there is no easily constructed inverse or pseudoinverse for their corresponding full operators, we use the adjoint of each operator normalized by factors of $(mN_f)^{-1}$ for the IBOS and $(mN_f^2)^{-1}$ for the JOBS—the extra N_f in the JBOS is to deal with the scaled DFT operator across frequency.

In Fig. 4 we can see that, when sub-sampled, all four proposed sampling operators are able to reconstruct the unknown matrix to reasonable accuracy. However, it is clear that the Rademacher IBOS and Rademacher JBOS sampling approaches perform slightly better than the IBOS and JBOS counterparts. Comparing to the Rademacher FFT approach as a baseline, we can see that none of the sampling operators perform nearly as well, and the roll off of the PTDs in the relative error is much more sharp for the Rademacher FFT. Unfortunately, the Rademacher FFT example is not possible to measure in NFTs, it is just a baseline method for comparison; its exceptional performance is expected since it has a guarantee that is, like Gaussian samples in CS, nearly optimal.

D. Multi-Frequency Reconstructions for a Horn Antenna

Next, in Fig. 5 we compare the performance of our proposed CS approaches for the simulated horn from Section IV-B in the presence of noise. As with the model representation error plots in Fig. 3, we also include the MMV approach. Without noise the results are highly similar and for the sake of brevity not included. For these experiments, we use $N_f = 200$, which amounts to 20 MHz samples, and window as described in Section IV-B. For the IBOS, JBOS, and MMV methods, we generate the measurements $\boldsymbol{W}$ using the set of known coefficients, from which we then randomly sub-select. This mimics typical single frequency measurements in that all we need for the IBOS and JBOS CS approaches are the sub-selected entries of $\boldsymbol{W}$ at the positions and frequencies specified by sampling the appropriate angle and frequency sample distributions, $w(\alpha_j, \beta_j, \gamma_j, f_j)$. For the Rademacher-based approaches, we directly generate the sub-sampled measurements of $\boldsymbol{Y}$. For the low-rank reconstructions, we use the same initialization approach as described in Section IV-C and a rank value of $r = 25$. For the QCBP results (labeled as ℓ_1), we use the SPGL1[8] software [59].

In the top row of Fig. 5, we see that each reconstruction approach recovers the horn antenna's WDFCs with at least 5% accuracy (roughly -25 dB) using $m \approx 0.4 N_{\text{sample}}^{\mu\pm=1} N_f$ or less, about 40% of all sample positions at each frequency (there about $2\, N_D^{\mu=\pm1}$ spatial sample positions, so this is $m \approx 0.8 N_D^{\mu=\pm1} N_f$ samples to recover $N_D^{\mu=\pm1} N_f$ unknowns). The IBOS ℓ_1 method and MMV approaches, with comparable performance, are the

[8]The use of this product is not an endorsement and is only to clarify what was used in this paper.

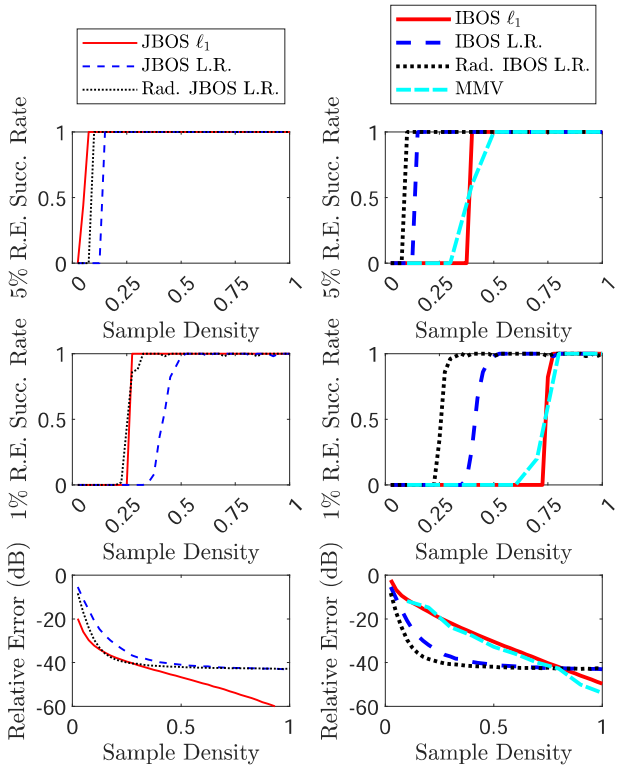

Fig. 5. *Noisy Horn Antenna Reconstructions* The reconstruction results for a simulated standard gain horn from 8–12 GHz. All plots share the legends given above the top panels (non-bold corresponds to the JBOS methods, left column, and bold corresponds to the IBOS or MMV methods, right column). The top two rows of plots give the success rate for 5% and 1% relative error (Success Rate $= \frac{\#\text{ of trials with R.E.}<\%\text{cutoff}}{\text{total \# of trials}}$ while the bottom two panels show the corresponding average relative errors. At each sample density, 50 trials are run for the proposed methods, while only 10 trials are used for the MMV method.

worst approaches; their standing among the other methods is as expected from the model representation errors Fig. 3. The JBOS ℓ_1 and Rademacher L.R. methods are the best, needing only $m \approx 0.1 N_{\text{sample}}^{\mu\pm=1} N_f$. The performance of the non-Rademacher low-rank methods come in slightly behind the JBOS ℓ_1 and Rademacher L.R. methods. Decreasing the success criteria to 1% relative error (-40 dB) in the second row of plots, we see that the IBOS ℓ_1 method requires roughly 75% of the conventional number of measurements, while the other methods fare better. The JBOS ℓ_1 and Rademacher L.R. approaches continue to perform the best, needing $m \approx 0.25 N_{\text{sample}}^{\mu\pm=1} N_f$ measurements. This means the best methods tested need roughly 0.5 measurements for each unknown, a significant savings considering conventional approaches need roughly 2 samples per unknown. Looking at the relative error, the JBOS ℓ_1 results corresponding to Theorem 8 perform the best over the broadest range of sample numbers. The stark difference between the IBOS or MMV and JBOS ℓ_1 results shows the vast improvement in model effectiveness the JBOS possesses over the other two. This is explained by the extra compression provided by the JBOS in Fig. 2 as well as the JBOS's improved theoretical performance over the IBOS from Section III.

As a note, the low-rank reconstruction approaches have accuracy limited by both the selected rank and the number of gradient descent iterations. In terms of the latter factor, experiments showed larger iteration numbers resulted in improved performance. We did not select these larger simulation iterations due to the large computation times needed to simulate many trials at each measurement number. However, when used in the wild, more iterations can be used, since single reconstructions are much less computationally burdensome than full phase diagrams. Moreover, the selected rank value can be optimized beyond what we considered here. One procedure to do this would be to use a holdout set of measurements, reconstruct under multiple assumed rank values in the BM approach (26), and use the rank value which gives the best predictive estimates for the holdout set of measurements.

V. Conclusion

Due to the long sample times, broadband nature of antenna or antenna array characterizations, and lack of existing multi-frequency reconstruction approaches, we proposed new multi-frequency compressive sensing approaches to that can be used in spherical near-field to far-field transformations or spherical holographic techniques. In particular, we proposed using a joint-sparse model for the Wigner D-function coefficients across the desired characterization band as well as a low-rank model. Numerical experiments showed that, for a simulated standard gain horn antenna, both models produce effective compression of the Wigner D-function coefficients beyond typical single frequency compressed sensing. We also saw that the effectiveness of each model depends on the density of desired frequency samples in the characterization band—higher density frequency samples improve both models' effectiveness while lower density frequency samples do the opposite. It is likely the case that the best model to use in applications will need to be tailored based on the desired frequency sample density. Future work can address more systematic approaches to model selection, or even combining the sparse and low-rank models to improve effectiveness.

For the joint-sparse approach we propose, we provided new BOS-based compressive sensing guarantees for multi-frequency spherical field measurements along with bounds on the sparse representation error for the joint-sparse model. These results only require monochromatic measurements, which means these guarantees apply in the context of existing measurement systems. We discussed the difficulty surrounding low-rank compressive sensing guarantees in the context of multi-frequency spherical NFTs using both monochromatic and polychromatic field measurements. The main constraint here is that measurements are in the form of a bounded orthonormal system for which no uniform low-rank compressive sensing guarantees exist, even with additional randomization as seen in our proposed Rademacher combined sampling schemes. Future work can aim to establish general low-rank compressive sensing guarantees for bounded orthonormal systems as seen in this work. In addition, future work could also aim to find alternative guarantees based on signal coherence, as is often done in the low-rank matrix sensing literature.

Our numerical experiments showed that both the joint-sparse and low-rank models provide effective approaches to recover an antenna's Wigner D-function coefficients in few compressive measurements. In particular, the JBOS ℓ_1 (monochromatic measurements) and the Rademacher-based low-rank (polychromatic measurements) approaches were able to recover the device's WDFCs to at least 5% or 1% (≈ -25 dB or -40 dB) relative error with a number of measurements that is around 0.1 or 0.25 times the conventional number of NFT samples, respectively. This is around 0.2 or 0.5 times the total unknowns, which is significant given conventional approaches require roughly 2 samples per unknown. The JBOS ℓ_1 approach, the only joint approach with an accuracy guarantee, showed the best performance in relative error. In contrast, for the case tested, the IBOS ℓ_1 approach (using the same measurements as the JBOS) was not sufficient to enable compressive reconstruction from less than 1/3 of the conventional number of NFT measurements. This may improve for devices with very high rates of sparsity/compression. However, in such cases we still expect the other proposed methods to provide better performance. Informally, if our observed gains extrapolate well to other devices that are more compressible at each individual frequency, IBOS ℓ_1 reconstruction may reduce measurements by say 1/2, but JBOS ℓ_1 reconstruction or Rademacher-based low-rank reconstruction could improve this further to 1/4 or better.

As noted at the end of our numerical experiments, the low-rank approaches were not optimized in terms of all possible parameters, in particular the selected rank and more gradient descent iterations. Thus, the effectiveness of the Rademacher sampling approaches, which may improve beyond what are even seen in this paper, imply that future research towards enabling such polychromatic measurements would be beneficial. Regardless, for the case where reconstruction guarantees are required, the monochromatic joint-sparse approach we present gives highly competitive results and could be of use in many labs today.

REFERENCES

[1] *IEEE Standard for Definitions of Terms for Antennas*, IEEE Standard145-2013 (Revision of IEEE Standard 145-1993), pp. 1–50, 2014.

[2] *User Equipment (UE) radio transmission and reception; Part 1: Range 1 Standalone*, Technical Specification 38.101-1 V18.2.0, 3rd Generation Partnership Project, Valbonne, France, Jun. 2023. [Online]. Available: https://www.3gpp.org/dynareport/38101-1.htm

[3] *User Equipment (UE) radio transmission and reception; Part 2: Range 2 Standalone*. Technical Specification 38.101-2 V18.2.0, 3rd Generation Partnership Project, Valbonne, France, Jun. 2023. [Online]. Available: https://www.3gpp.org/dynareport/38101-2.htm

[4] *IEEE recommended practice for antenna measurements*, IEEE Standard 149-2021 (Revision of IEEE Standard 149-1977), pp. 1–207, 2022.

[5] *IEEE Recommended Practice for Near-Field Antenna Measurements*, IEEE Standard 1720-2012, pp. 1–102, 2012.

[6] E. S. Gillespie, "Special issue on near-field scanning techniques," *IEEE Trans. Antennas Propag.*, vol. 36, no. 6, pp. 725–901, 1988.

[7] C. Culotta-López, D. Heberling, A. Bangun, A. Behboodi, and R. Mathar, "A compressed sampling for spherical near-field measurements," in *Proc. 2018 AMTA Proc.*, Nov. 2018, pp. 1–6.

[8] B. Hofmann, O. Neitz, and T. Eibert, "On the minimum number of samples for sparse recovery in spherical antenna near-field measurements," *IEEE Trans. Antennas Propag.*, vol. 67, no. 12, pp. 7597–7610, Dec. 2019.

[9] *Study on test methods*. Tech. Rep. 38.810 V16.7.0, 3rd Generation Partnership Project, Valbonne, France, Jun. 2023. [Online]. Available: https://www.3gpp.org/dynareport/38810.htm

[10] CTIA, "Test plan for wireless device over-the-air performance," *Cellular Telecommun. Internet Assoc.*, vol. 3.8.2, pp. 1–628, Apr. 2019.

[11] M. Guler and E. Joy, "High resolution spherical microwave holography," *IEEE Trans. Antennas Propag.*, vol. 43, no. 5, pp. 464–472, May 1995.

[12] Y. Rahmat-Samii and J. Lemanczyk, "Application of spherical near-field measurements to microwave holographic diagnosis of antennas," *IEEE Trans. Antennas Propag.*, vol. 36, no. 6, pp. 869–878, Jun. 1988.

[13] J. E. Hansen, *Spherical Near-Field Antenna Measurements*. London, U.K.: The Inst. Eng. Technol., Jun. 1988.

[14] D. Löschenbrand and C. Mecklenbrauker, "Fast antenna characterization via a sparse spherical multipole expansion," in *Proc. 4th Int. Workshop Compressed Sens. Theory Its Appl. Radar, Sonar Remote Sens.*, Sep. 2016, pp. 212–216.

[15] B. Verdin and P. Debroux, "Sparese matrix motivated reconstruction of far-field radiation patterns," *US Army Res. Lab.*, Rep. ARL-TR-7255, pp. 1–30, Mar. 2015.

[16] R. Cornelius, D. Heberling, N. Koep, A. Behboodi, and R. Mathar, "Compressed sensing applied to spherical near-field to far-field transformation," in *Proc. 10th Eur. Conf. Antennas Propag.*, 2016, pp. 1–4.

[17] B. Fuchs, L. Le Coq, S. Rondineau, and M. Migliore, "Compressive sensing approach for fast antenna far field characterization," in *Proc. 12th Eur. Conf. Antennas Propag.* 2018, pp. 1–5.

[18] A. Bangun, A. Behboodi, and R. Mathar, "Sensing matrix design and sparse recovery on the sphere and the rotation group," *IEEE Trans. Signal Process.*, vol. 68, pp. 1439–1454, 2020.

[19] M. Valdez, A. Yuffa, and M. Wakin, "Compressive sensing with wigner D-Functions on subsets of the sphere," *IEEE Trans. Signal Process.*, vol. 70, pp. 5652–5667, 2022.

[20] J. Rockway, J. Meloling, and J. C. Allen, "Interpolating spherical harmonics for computing antenna patterns" Space Naval Warfare Syst. Center Pacific, Tech. Rep. 1999, Jul. 2011.

[21] H. Rauhut and R. Ward, "Sparse recovery for spherical harmonic expansions," Feb. 2011, *arXiv:1102.4097*.

[22] H. Rauhut and R. Ward, "Sparse legendre expansions via l1-minimization," *J. Approx. Theory*, vol. 164, no. 5, pp. 517–533, May 2012.

[23] M. Valdez, J. Rezac, and M. Wakin, "Quadrature-based compressive sensing guarantees for bounded orthonormal systems," vol. 7, 2024.

[24] M. Don and G. Arce, "Antenna radiation pattern compressive sensing," in *Proc. MILCOM 2018-2018 IEEE Mil. Commun. Conf.*, 2018, pp. 174–181.

[25] M. Don, "Compressive antenna pattern measurement: A case study in practical compressive sensing," in *Proc. 2022 IEEE AUTOTESTCON*, Aug. 2022, pp. 1–9.

[26] S. Cotter, B. Rao, K. Engan, and K. Kreutz-Delgado, "Sparse solutions to linear inverse problems with multiple measurement vectors," *IEEE Trans. Signal Process.*, vol. 53, no. 7, pp. 2477–2488, Jul. 2005.

[27] J. Chen and X. Huo, "Theoretical results on sparse representations of multiple-measurement vectors," *IEEE Trans. Signal Process.*, vol. 54, no. 12, pp. 4634–4643, Dec. 2006.

[28] D. Baron, M. F. Duarte, M. B. Wakin, S. Sarvotham, and R. G. Baraniuk, "Distributed compressive sensing," Jan. 2009, *arXiv:0901.3403*.

[29] M. F. Duarte and Y. C. Eldar, "Structured compressed sensing: From theory to applications," *IEEE Trans. Signal Process.*, vol. 59, no. 9, pp. 4053–4085, Sep. 2011.

[30] M. Davenport and J. Romberg, "An overview of low-rank matrix recovery from incomplete observations," *IEEE J. Sel Top Signal Process.*, vol. 10, no. 4, pp. 608–622, Jun. 2016.

[31] C. Li, T. Sun, K. Kelly, and Y. Zhang, "A compressive sensing and unmixing scheme for hyperspectral data processing," *IEEE Trans. Image Process.*, vol. 21, no. 3, pp. 1200–1210, Mar. 2012.

[32] G. Martín, J. Bioucas-Dias, and A. Plaza, "HYCA: A new technique for hyperspectral compressive sensing," *IEEE Trans. Geosci. Remote Sens.*, vol. 53, no. 5, pp. 2819–2831, May 2015.

[33] M. Davies and Y. Eldar, "Rank awareness in joint sparse recovery," *IEEE Trans. Inf. Theory*, vol. 58, no. 2, pp. 1135–1146, Feb. 2012.

[34] Y. Liu, "Universal low-rank matrix recovery from Pauli measurements," in Proc. *Adv. Neural. Inf. Process. Syst.*, vol. 24. 2011.

[35] H. Rauhut, R. Schneider, and Ž. Stojanac, "Low rank tensor recovery via iterative hard thresholding," *Linear Algebra Appl.*, vol. 523, pp. 220–262, Jun. 2017.

[36] S. Oymak, B. Recht, and M. Soltanolkotabi, "Isometric sketching of any set via the restricted isometry property," *Inf. Inference: J. IMA*, vol. 7, no. 4, pp. 707–726, Dec. 2018.

[37] S. Oymak, A. Jalali, M. Fazel, Y. Eldar, and B. Hassibi, "Simultaneously structured models with application to sparse and low-rank matrices," *IEEE Trans. Inf. Theory*, vol. 61, no. 5, pp. 2886–2908, May 2015.
[38] K. Lee, Y. Wu, and Y. Bresler, "Near-optimal compressed sensing of a class of sparse low-rank matrices via sparse power factorization," *IEEE Trans. Inf. Theory*, vol. 64, no. 3, pp. 1666–1698, Mar. 2018.
[39] C. Balanis, *Antenna Theory: Analysis and Design*, 4th ed. Hoboken, New Jersey, USA: Wiley, Feb. 2016.
[40] D. A. Varshalovich, A. N. Moskalev, and V. K. Khersonskii, *Quantum Theory of Angular Momemtum*. New Jersey, USA: World Scientific, Oct. 1988.
[41] U. Haagerup and H. Schlichtkrull, "Inequalities for jacobi polynomials," *Ramanujan J.*, vol. 33, no. 2, pp. 227–246, Feb. 2014.
[42] N. Gumerov and R. Duraiswami, "Recursive computation of spherical harmonic rotation coefficients of large degree," in *Excursions in Harmonic Analysis*, vol. 3, R. Balan, M. Begué, J. Benedetto, W. Czaja, and K. Okoudjou, Eds., Switzerland: Birkhäuser, 2015, pp. 105–141.
[43] P. A. Martin, *Multiple Scattering: Interaction of Time-Harmonic Waves With N Obstacles*, (Ser. Encyclopedia of Mathematics and Its Applications). Cambridge, U.K.: Cambridge Univ. Press, 2006.
[44] B. Bean, "The radio refractive index of air," *Proc. IRE*, vol. 50, no. 3, pp. 260–273, 1962.
[45] S. Foucart and H. Rauhut, *A Mathematical Introduction to Compressive Sensing*. Basel, Switzerland: Birkhäuser, 2013.
[46] Z. Khalid, S. Durrani, R. A. Kennedy, Y. Wiaux, and J. D. McEwen, "Gauss-Legendre sampling on the rotation group," *IEEE Signal Process. Lett.*, vol. 23, no. 2, pp. 207–211, Feb. 2016.
[47] D. L. Donoho, "Compressed sensing," *IEEE Trans. Inf. Theory*, vol. 52, no. 4, pp. 1289–1306, Apr. 2006.
[48] E. Candes and T. Tao, "Decoding by linear programming," *IEEE Trans. Inf. Theory*, vol. 51, no. 12, pp. 4203–4215, Dec. 2005.
[49] E. Candes, J. Romberg, and T. Tao, "Robust uncertainty principles: Exact signal reconstruction from highly incomplete frequency information," *IEEE Trans. Inf. Theory*, vol. 52, no. 2, pp. 489–509, Feb. 2006.
[50] E. Candes and T. Tao, "Near-optimal signal recovery from random projections: Universal encoding strategies?," *IEEE Trans. Inf. Theory*, vol. 52, no. 12, pp. 5406–5425, Dec. 2006.
[51] H. Rauhut, "Random sampling of sparse trigonometric polynomials," *Appl. Comput. Harmon. Anal.*, vol. 22, no. 1, pp. 16–42, Jan. 2007.
[52] M. Rudelson and R. Vershynin, "On sparse reconstruction from fourier and Gaussian measurements," *Commun. Pure Appl. Math.*, vol. 61, no. 8, pp. 1025–1045, 2008.
[53] N. Burq, S. Dyatlov, R. Ward, and M. Zworski, "Weighted eigenfunction estimates with applications to compressed sensing," *SIAM J. Math. Anal.*, vol. 44, no. 5, pp. 3481–3501, Jan. 2012.
[54] P. Jain, R. Meka, and I. Dhillon, "Guaranteed Rank Minimization Via Singular Value Projection," in *Proc. Adv. Neural Informat. Process. Syst.*, vol. 23, 2010.
[55] Z. Zhu, Q. Li, G. Tang, and M. Wakin, "The global optimization geometry of low-rank matrix optimization," *IEEE Trans. Inf. Theory*, vol. 67, no. 2, pp. 1308–1331, Feb. 2021.
[56] H. Rauhut and U. Terstiege, "Low-rank matrix recovery via rank one tight frame measurements," *J. Fourier Anal. Appl.*, vol. 25, no. 2, pp. 588–593, Apr. 2019.
[57] M. Valdez, A. Yuffa, and M. Wakin, "On-grid compressive sampling for spherical field measurements in acoustics," *J. Acoustical Soc. Amer.*, vol. 152, no. 4, pp. 2240–2256, Oct. 2022.
[58] F. Mezzadri, "How to generate random matrices from the classical compact groups," *Notices Amer. Math. Soc.*, vol. 54, no. 5, pp. 592–604, 2007.
[59] E. van den Berg and M. P. Friedlander, "SPGL1: A solver for large-scale sparse reconstruction," Dec. 2019. [Online]. Available: https://friedlander.io/spgl1